Int. J. Electrochem. Sci., 17 **(2022)** Article Number: 221059, doi: 10.20964/2022.10.58

International Journal of
ELECTROCHEMICAL
SCIENCE
www.electrochemsci.org

Electrochemical Behavior of Phoenix tree leaves derived Porous Carbon Material as Electrode for Supercapacitors

Feifei Yu[1,*], *Fenglan Wang*[1], *Yanzhang Yang*[2]

[1] School of Mechanical Engineering, Shenyang University, Shenyang, Liaoning 110044, China
[2] Shenyang Kedao Instrument Co., Ltd, Shenyang, Liaoning 110044, China
[*]E-mail: yuyufeifeiengineer@163.com

Received: 3 July 2022 / *Accepted:* 24 August 2022 / *Published:* 10 September 2022

Due to the limitation of hydrolysis voltage, the operating voltage of aqueous electrolyte-based supercapacitors generally does not exceed 1.2 V, which severely limits the application of aqueous supercapacitors. In fuel cell vehicles (FCV), supercapacitors are generally used as peaking power sources (PPS) with an aqueous electrolyte. In this study, an ultra-capacitive/oxygen reduction bifunctional electrode material was designed and prepared as a fuel cell cathode material to realize the functions of fuel cell and PPS in the same electrochemical cell, thus simplifying the structure of the FCV energy subsystem. In this work, a porous material (PC) was prepared by hydrothermal carbonization with phoenix tree leaves being a carbon source. PC has an oxygen reduction electrocatalytic activity similar to commercial 30 wt.% Pt/C. The change in electrode potential is accompanied by the generation of a charging current, the magnitude of which is related to the rate of change of electrode potential. Using PC as a fuel cell cathode material is expected to simplify the structure of the FCV energy subsystem.

Keywords: Supercapacitors; Porous carbon materials; Fuel cells vehicles; Hydrothermal carbonization; KOH activation

1. INTRODUCTION

Ultracapacitors are electrochemical energy storage devices with extremely high capacities. The capacitance of conventional capacitors often reaches only microfarads and millifarads, while supercapacitors can reach even hundreds of farads, which mainly comes from the high material-specific surface area, the minimal bilayer spacing and the high dielectric constant. Supercapacitors store/release electrical energy by charging/releasing at the electrode-electrolyte interface and are well suited for high-power applications [1–3]. Ultracapacitors have very fast charge and discharge rates like conventional capacitors, but their specific energy is lower than that of batteries. Supercapacitors can store/release charge highly reversibly and quickly, for the reason that no slow chemical processes or phase changes

occur during their charging/discharging process. Compared with electrochemical batteries, supercapacitors have the advantages of long cycle life, high efficiency, and no memory effect [4,5], in addition to a high specific power. These features make supercapacitors quite promising for electric vehicles, backup power systems, and mobile communications applications, attracting extensive attention [6].

Activated carbon is the most commonly used active material in double-layer capacitors, which has a high specific surface area and relatively low price [6,7]. Activated carbon is usually produced by physical or chemical activation, and the raw materials can be carbonaceous materials from various sources (e.g. wood, coal, etc.). The physical activation method usually involves heat treatment of carbon precursors in an oxidizing atmosphere (air, water vapour, CO_2, etc.). For the chemical activation method, the heat treatment is carried out at a lower temperature with activators, such as KOH, NaOH, ZnCl and H_3PO_4. Activated carbons have different physicochemical properties and high surface area depending on the activation method and the carbon precursor used [8,9]. The activation process produces a rich pore structure in activated carbons [10]. In principle, the specific capacity of activated carbon materials is positively correlated with their specific surface area [11]. However, the relationship is unclear in practice, and some studies have shown that the relationship is not necessarily linear. Some activated carbons with high specific surface areas are likely to have a relatively small specific capacitance, suggesting that not all surfaces can be used to store charges [12]. Therefore, while the comparative area is an important factor in the performance of electric double layer capacitors, other factors affecting the electrochemical performance should also be considered, such as the pore size distribution [13]. In addition, excessive activation leads to large pore volumes, resulting in drawbacks such as low conductivity and material density, which also causes a decrease in energy density and power density.

Due to the depletion of global fossil fuel, environmental pollution and greenhouse effect become increasingly serious, the sustainable development of human society and economy is greatly affected. In recent years, the development of electric vehicles (EVs), hybrid electric vehicles (HEVs) and fuel cell vehicles (FCVs), with the advantages of energy saving and environmental protection, has received significant attention [14–17]. Fuel cell is an advanced clean energy source that directly converts chemical energy into electrical energy, with high efficiency and low emissions. However, due to the low power density of fuel cells, vehicles using only fuel cells cannot meet the need of practical applications, which is the reason why electric vehicles were invented before internal combustion engine vehicles but have not been popularized [18,19]. One possible solution is to couple a fuel cell with a peak power supply (PPS). Supercapacitors are generally used as PPSs, which are connected in parallel with fuel cells as energy supply systems. Fuel cells provide electrical power and operate in a narrow power range. The FCV causes power fluctuations during the start-stop phase and acceleration/deceleration, which is absorbed by the supercapacitor and the control circuit controls the current flow [20,21].

In supercapacitor applications, water-based electrolytes are limited in energy density by relatively low decomposition voltages. However, their strengths of high ionic conductivity, inexpensiveness and the fact that the manufacturing process does not require waterproofing or inert atmosphere protection make them advantageous for high-power applications [22]. In addition, the specific capacity of carbon in aqueous electrolytes is much higher than that in non-aqueous solvents. Moreover, water-based electrolytes have advantages in high-power applications, which meets the

requirements of PPS. Carbon-based electrode materials in aqueous fuel cells are currently a widely-discussed research topic, thus it is well worth exploring the integration of ultra-capacitors and fuel cells within a single electrochemical cell as a way to simplify the energy subsystem of FCV.

2. EXPERIMENTAL

2.1. Chemicals and instruments

Phoenix tree leaves were collected from the campus of Shenyang University. Anhydrous ethanol, phosphoric acid and N-methylviologenone were purchased from Sinopharm Chemical Reagent Co. Polyvinylpyrrolidone was purchased from Shanghai Aorun Chemical. Diphenylcarbonyl diphosphate was purchased from Shanghai Kexing Trading Co. All other chemicals were analytical grade and used without further purification.

The structural characterization of the materials was carried out with a D8 advance type X-ray diffractometer. The radiation source of the X-ray diffractometer was a CuKα target. The operating condition was 40 kV/40 mA, the wavelength was 0.15406 nm, the scanning range was 59-80°, the scanning speed was 2 deg/min, the accuracy was <0.02°, and the scanning measurement accuracy was 0.0001°.

The infrared spectroscopy test was characterized with a NEXUS 670 FTIR spectrometer. Before the test, the dried sample to be tested and the potassium bromide powder should be well mixed at a mass ratio of 1:100 and then put into the preparation mold and pressed with a tablet press. The prepared sample was put into the infrared scanning area and measured in the wavelength range of 500~4000 cm^{-1}.

The instrument used for the SEM test in this paper was a JEOLJSM-6700F scanning electron microscope, which was adopted to observe the surface morphology of carbon materials.

2.2. Preparation of porous carbon and activization

The collected phoenix tree leaves were first washed and dried before being ball-milled. An appropriate amount of phoenix tree leaf powder was weighed and evenly dispersed in distilled water, which was then poured into the hydrothermal reactor. An appropriate amount of dilute hydrochloric acid was added to adjust the pH. After sealing, the reactor was put in an oven to be heated and kept warm. After the reaction is finished, the reactor was cooled to room temperature. The reaction solution was taken out, extracted, filtered, washed and dried to obtain a dark brown powder. A certain amount of hydrothermal carbon material was placed in an appropriate KOH solution and put into a tube furnace for activation. After cooling to room temperature, the product was removed, washed with an acid solution, extracted, filtered, and dried to obtain porous biomass porous carbon material powder (denoted as PC).

2.3. *Electrochemical characterization*

Preparation of porous carbon material working electrode: porous carbon material, acetylene black and polyvinylidene fluoride were mixed in the mass ratio of 8:1:1. Firstly, the porous carbon

material and acetylene black were dispersed in an ethanol solution, and the homogeneously mixed powder was obtained by constant stirring. Poly (vinylidene fluoride) was dissolved in nitrogen methyl pyrrolidone to obtain a mixed solution. The mixed powder was then uniformly dispersed into the mixed solution to obtain the slurry, which was coated on a 1 × 2 cm nickel grid and dried at 60°C for 8 h. After the mixture was pressed onto the nickel grid with a press, the working electrode was obtained by continuing to dry at 120°C for 6 h. During the electrochemical performance test, a three-electrode system with porous carbon material being the working electrode, saturated glycury electrode being the reference electrode and platinum sheet electrode being the counter electrode was utilized. The cyclic voltammetry test was carried out on a Shanghai Chenhua CHI604 electrochemical workstation with a scan voltage range of -0.8- 0.2 V and a scan rate of 10- 200 mV/s.

3. RESULTS AND DISCUSSION

Figure 1 shows the XRD patterns of the carbon materials prepared with the hydrothermal method. As presented in the figure, the XRD spectrum of phoenix tree leaves shows four diffraction peaks at 20=15.29°, 24.36°, 30.84°, and 35.98°, which represent the (110), (020), (220), and (112) crystallographic planes of calcium oxalate [23], respectively, indicating that many calcium oxalate impurities are contained in the phoenix tree leaves. As shown in the XRD spectra of the carbon materials after hydrothermal carbonization, the diffraction peaks of calcium oxalate impurities disappear [24], which results from the addition of an appropriate amount of hydrochloric acid to the hydrothermal reaction system, thus the impurities in the phoenix tree leaves could be dissolved in water and removed [25]. In addition, the presence of a broad diffraction peak from 10° to 30°, which corresponds to the (002) crystal plane of graphite, can be observed in the figure, indicating that the formed carbon is amorphous structured and already has a certain tendency to graphitize.

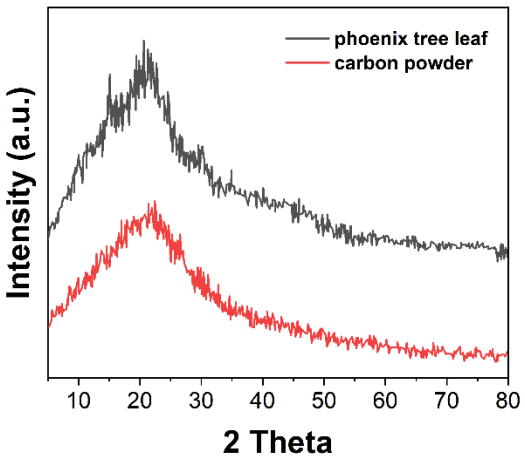

Figure 1. XRD patterns of powder of phoenix tree leaves and carbon powder synthesized by hydrothermal method.

Figure 2 shows the FTIR spectra of phoenix tree leaves and hydrothermal carbon materials. It can be observed from the figure that phoenix tree leaves retain their general characteristics after hydrothermal charring. It can also be found that the absorption peak of the product at 3200-3500 cm^{-1} is significantly weakened, which indicates that the hydroxyl groups presented in phoenix tree leaves reacted during the hydrothermal reaction [26]. The absorption peaks with wave numbers in the range of 1000-1450 cm^{-1} correspond to the stretching vibrations of esters, hydroxyl groups and ethers as well as the bending vibrations of OH [27]. It shows that the phoenix tree leaves underwent dehydration, condensation, and aromatization during hydrothermal. The absorption peaks at 1729 cm and 1611 cm^{-1} can be attributed to C=C (aromatic ring) vibrational peak and C=O (ester, carboxyl or coupon group) vibrational peak [28], among which the intensity of the C=O vibrational peak increases after hydrothermal treatment, indicating that the surface active functional groups increase after hydrothermal treatment, and the functionality of the carbon material is enhanced [29].

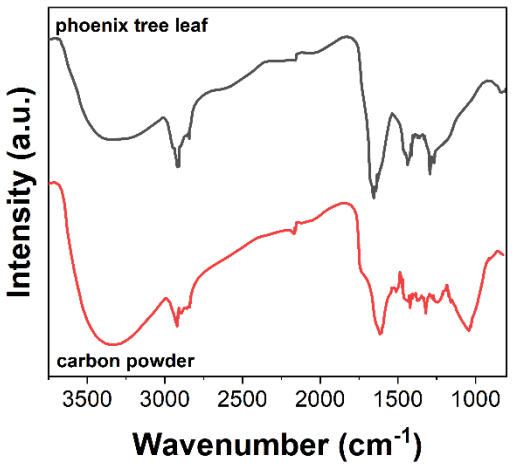

Figure 2. FTIR spectra of phoenix tree leaves and carbon powder synthesized by hydrothermal method.

Figure 3A shows the SEM image of phoenix tree leaf powder. It can be seen from the figure that the powder of phoenix tree leaves is irregularly lumpy, and the particle size varies. Figure 3B presents the SEM image of the carbon material prepared by hydrothermal reaction, from which it is observed that the phoenix tree leaves treated by hydrothermal obtaining can form spherical particles with a particle size of 2-4 μm, which is consistent with the general reaction mechanism of preparing biomass carbon microspheres with hydrothermal method. First, the polysaccharides contained in phoenix tree leaves undergo hydrolysis and turn into glucose at a specific temperature. Afterwards, the glucose undergoes a dehydration condensation reaction to produce aromatic compounds and oligomers. When the reaction reaches a critical supersaturation level, the aromatic compounds, macromolecules containing carboxylic acid groups and oligomers are further dehydrated to form nuclei. Eventually, the nuclei cross-link and polymerize with each other to form carbon microspheres [30].

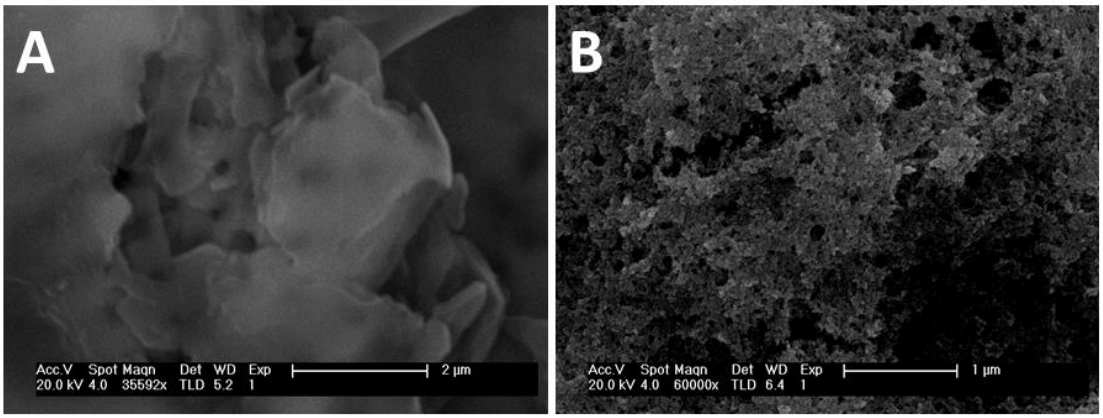

Figure 3. SEM images of (A) phoenix tree leaves and (B) carbon powder synthesized by hydrothermal method.

To characterize the oxygen reduction electrocatalytic activity of carbon powder and PC, CV and line sweep voltammetry (LSV) tests were performed, and the test results are shown in Figure 4. Figure 4A presents the LSV curves for carbon powder, PC and commercial 30 wt.% Pt/C at a sweep rate of 10 mV/s. For the LSV test of PC obtained after activation, E_o is at -0.08 V, at which time the electrochemical step controls the electrode reaction rate [31,32]. The current keeps increasing with the negative potential sweep, and the reaction rate is controlled by the electrochemical and mass transfer steps. The current no longer increases after -0.28 V, and the mass transfer step controls the reaction. The current density at this point is called the ultimate diffusion current density (I_d), and the value of Id for PC is 5.0 mA/cm^2. Under the same test conditions, the LSV test curves for PC and 30 wt.% Pt/C show similar trends, with the oxygen reduction onset potential and ultimate current density being very close [33,34]. These results indicate that the catalytic activity of PC catalyst for oxygen reduction is similar to that of 30 wt.% Pt/C. For carbon powder, E_o negatively shifts to -0.13 V. A current plateau comes after the potential scan reaches -0.3 V, but it does not appear.

From the CV plot in Figure 4B, it can be seen that the CV curve of PC in N_2-saturated 0.1 M KOH electrolyte is rectangular, indicating that no electrochemical reaction occurs [35]. After the electrolyte is saturated with O_2, the CV curve shows a clear reduction peak at around -0.227 V, corresponding to the reduction reaction of O_2 and being negatively shifted concerning the reduction peak of 30 wt.% Pt/C (-0.176 V). It indicates that the oxygen reduction reaction can proceed efficiently under the catalysis of PC [36,37]. Under the same conditions, the reduction peak of carbon powder (-0.268 V) is negatively shifted concerning PC, indicating that the oxygen reduction catalytic activity of carbon powder is inferior to that of PC, which is in line with the result of LSV test.

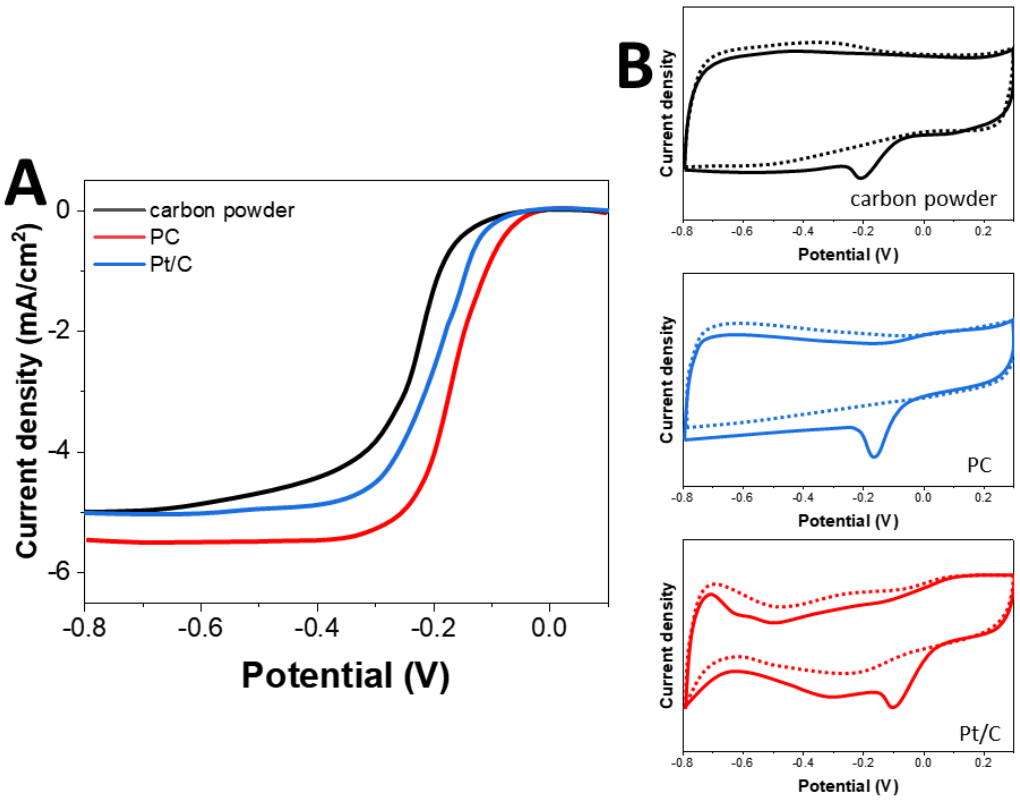

Figure 4. (A) LSV (10 mV/s) and (B) CV (50 mV/s) of carbon powder, PC and commercial 30 wt.%Pt/C catalyst in 0.1 M KOH.

To further investigate the kinetic process of PC-catalyzed oxygen reduction, rotating ring-disk electrode (RRDE) tests were performed on PC and commercial 30 wt.% Pt/C catalysts. The ring current and disk current information of the RRDE tests for PC and Pt/C are presented in Figure 5A-B, respectively. As seen from Figure 5A, the trend of the magnitude of the ring currents of PC and Pt/C are similar, and the ring currents of both are in the same order of magnitude in the potential range of 0~-0.8V. With the negative sweep of the potential, the ring current plateaus at about 0.3 V, lagging the RDE test by about 0.6 V. The results of the disk electrode test shown in Figure 5B are consistent with those of the RDE test. The number of electrons transferred n and HO_2-yields during the PC and Pt/C catalyzed oxygen reduction reactions are given in Figure 5C-D, respectively. In the potential range of -0.2 to -0.8 V, the number of electrons transferred in the PC-catalyzed oxygen reduction reaction is above 3.60, and the HO_2-yield remains below 10%, which increases gradually with the negative sweep of the potential [38,39]. The above analysis shows that when PC is used as a cathodic oxygen reduction catalyst, the HO yield is low in the potential range of -0.2 V to -0.8 V, and the catalytic reaction can proceed relatively stably [40].

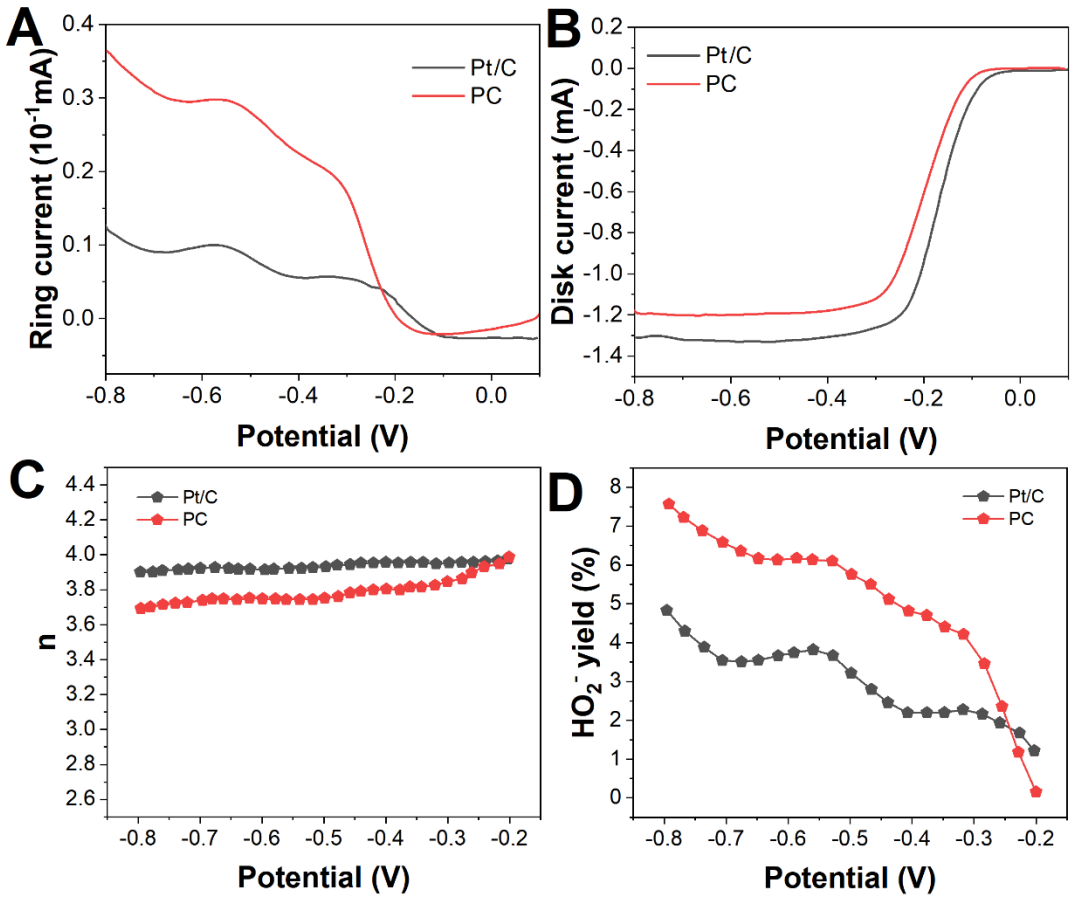

Figure 5. (A) Ring current, (B) disk current, (C) number of transferred electrons, (D) hydrogen peroxide yield of PC and commercial 30 wt.%Pt/C catalyst in 0.1 M KOH.

In order to investigate the supercapacitance performance of PC, its electrochemical performance was examined with the CV and GCD tests in 6 M aqueous KOH solution. Figure 6A shows the CV curves of PC at different potential scan rates. At a scan rate of 5 mV/s, the CV curves present a more desirable rectangular shape and no significant Faraday currents, indicating that the PC has no significant pseudocapacitance [41]. At a scan rate of 20 mV/s, the CV curve shape does not change significantly. The CV curve is slightly polarized at a scan rate of 50 mV/s, while at a scan rate of 100 mV/s, the CV curve is more severely polarized. Figure 6B shows the GCD curves of PC at different current densities. The IR of the GCD curves at different charge and discharge current densities is very small, and the calculated ESR is about 1.0 Ω. The internal resistance of the active material is less than 1.0 Ω, indicating that the material has good conductivity [41,42]. The charging time and discharging time are equal, which indicates that the Coulomb efficiency is high. The voltage varies with time, showing an obvious linear relationship, which is a typical characteristic of double layer capacitor. The specific capacity of PC reaches 269 F/g at 1A/g current density. 194 F/g is still available at 20 A/g current density. The above results indicate that the PC electrode material has good bilayer capacitance performance with high reversibility [43]. Compared with related references (Table 1), it can be found that the PC in this work has a competitive specific capacitance and power storage performance.

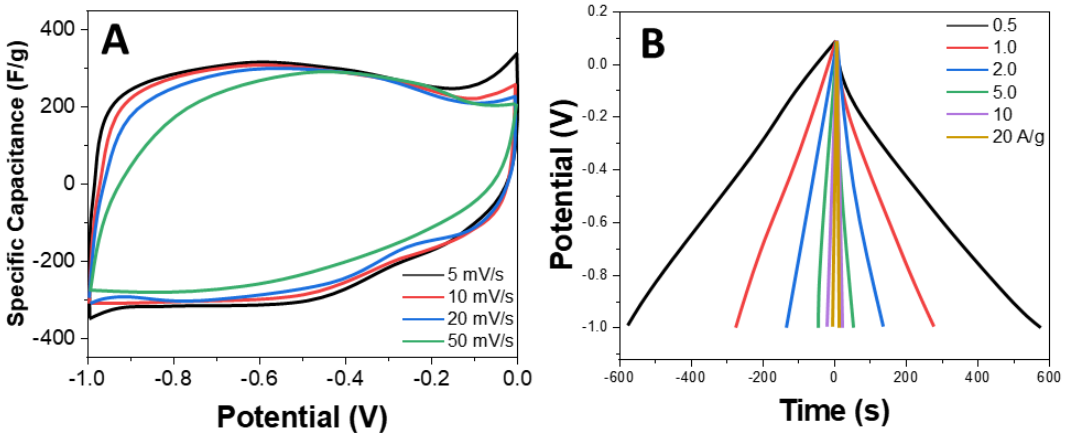

Figure 6. (A) CV and (B) GCD of PC in 6 M KOH.

Table 1. The comparison of the capacity performances of this work with references.

Electrode	Electrolyte	Current density (A/g)	Specific capacitance (F/g)	Reference
Cabbage leaves	6 M KOH	1	204	[44]
Sugarcane bagasse	1 M H_2SO_4	1	298	[45]
Sunflower seed shells	6 M KOH	0.25	311	[46]
Starch	6 M KOH	0.10	277	[47]
PC	6 M KOH	1	269	This work

The high-current performance of supercapacitors relies heavily on the rapid migration of load ions in the electrolyte, thus the carrier concentration has a huge impact on the performance of supercapacitors. In this work, a mixture of 0.1 M KOH and 5 M NaCl was chosen as electrolytes to maximize the carrier concentration [48]. Figure 7A shows the CV curves of PC at different potential scan rates. It can be seen that the polarization of the CV curves is significantly improved. Figure 7B shows the GCD curves of PC at different current densities. It can be seen that the IR of the GCD curve is significantly reduced, which indicates that the ESR of the system is significantly reduced. The above results reveal that increasing the carrier concentration of the electrolyte can effectively improve the performance of the supercapacitor. However, due to the toxic effect of CO_2 on KOH solution, the KOH concentration in alkaline hydroxide fuel cells should not be too high. Cl^- has an extremely strong corrosive effect, and it is not suitable to add a large amount of chlorine salt to the electrolyte, thus further study is needed on finding a suitable strategy to increase the carrier concentration of the electrolyte [49].

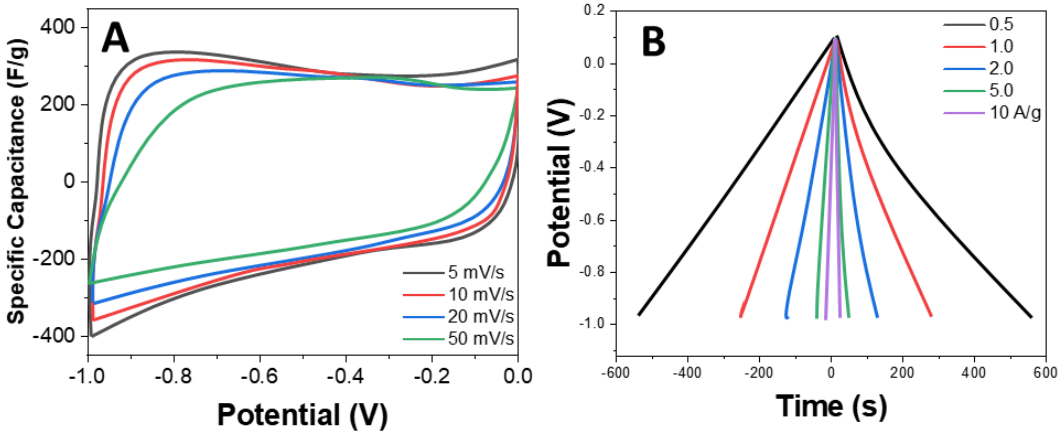

Figure 7. (A) CV and (B) GCD of PC in 0.1 M KOH and 5 M NaCl mixture electrolyte.

In this study, a step potential was further applied to the working electrode from the open-circuit state in an oxygen-saturated 0.1 M KOH aqueous solution to simulate the starting phase of an electric vehicle to study the relationship between the system current, the step potential and time. Figure 8A shows the current-time curve when the step potential is -0.1 V. It can be seen that the system passes a very large current at the beginning and decreases sharply within 0.5 s. After that, the current gradually stabilizes and remains small, with the peak current being about 8 times the intensity of the steady current [50,51]. The high current at the beginning of the test comes from the superposition of the charging current of the bilayer capacitance on the electrode surface and the cathodic oxygen reduction current [52,53]. As the bilayer equilibrium is established, the charging current disappears rapidly, and the cathodic oxygen reduction current provides the system current [54]. Figure 8B presents the current time curve for a step potential of -0.2 V. It can be noted that the system passes a very large current at the beginning and decreases sharply within 0.2 s, after which the current decrease slows down. After 5.0 s, the current gradually stabilizes and remains at a small value, with the peak current being about 9 times the intensity of the steady current [55,56]. The high current in the initial stage comes from the superposition of the charging current of the bilayer capacitance on the electrode surface and the cathodic oxygen reduction current. With the establishment of the bilayer equilibrium, the charging current disappears rapidly, and the cathodic oxygen reduction current supplies the system current [57]. As shown in Figure 8A, at an electrode potential of -0.2 V, the oxygen reduction reaction is controlled by electrochemical and mass transfer processes. On the one hand, the slow diffusion mass transfer processes prevent the reactants on the electrode surface from replenishing in time. On the other hand, the slower electrochemical process cannot rapidly consume the reactants on the electrode surface to establish mass transfer equilibrium. As a result, the concentration of reactants on the electrode surface slowly decreases and the reaction rate slowly decreases as well, manifested as a slight decrease in the cathodic current. Figure 8C shows the current time curve for a step potential of -0.3 V. It can be seen that the trend of current change is similar to Figure 8A. The current decreases sharply in 2.0 s and then stabilizes, and the peak current is about 21 times the intensity of the steady current. Figure 8A reveals that the oxygen reduction reaction is under

the control of the mass transfer process at an electrode potential of -0.3 V. The fast electrochemical process allows the reactants on the electrode surface to be consumed rapidly and establishes the mass transfer equilibrium [58]. As a result, the concentration of reactants on the electrode surface is rapidly stabilized, and the reaction rate is subsequently stabilized, as shown by the rapid stabilization of the cathodic current. Figure 8D shows the current time curve when the step potential is -0.4V. It can be found that the current variation trend is similar to Figure 8A. The current decreases sharply in 1.0 s and then stabilizes, with the peak current being about 35 times the intensity of the steady current. The system current rapidly stabilizes at a step potential of -0.4 V after the bilayer charging is completed. The above results and analysis reveal that the system can provide a charging current much larger than the electrode reaction Faraday current within a short time of the electrode potential change due to the existence of the bilayer capacitive property of the electrode material. In addition, the faster the electrode potential changes, the higher the charging current is. This charging current can provide a high starting current during the start-up phase of an electric vehicle to meet its large starting torque requirements. Morevoer, the current fluctuations caused by load power changes can be absorbed as a charging current, reducing the change in electrode potential, which allows the battery to operate in a relatively stable voltage range, thus extending the battery life.

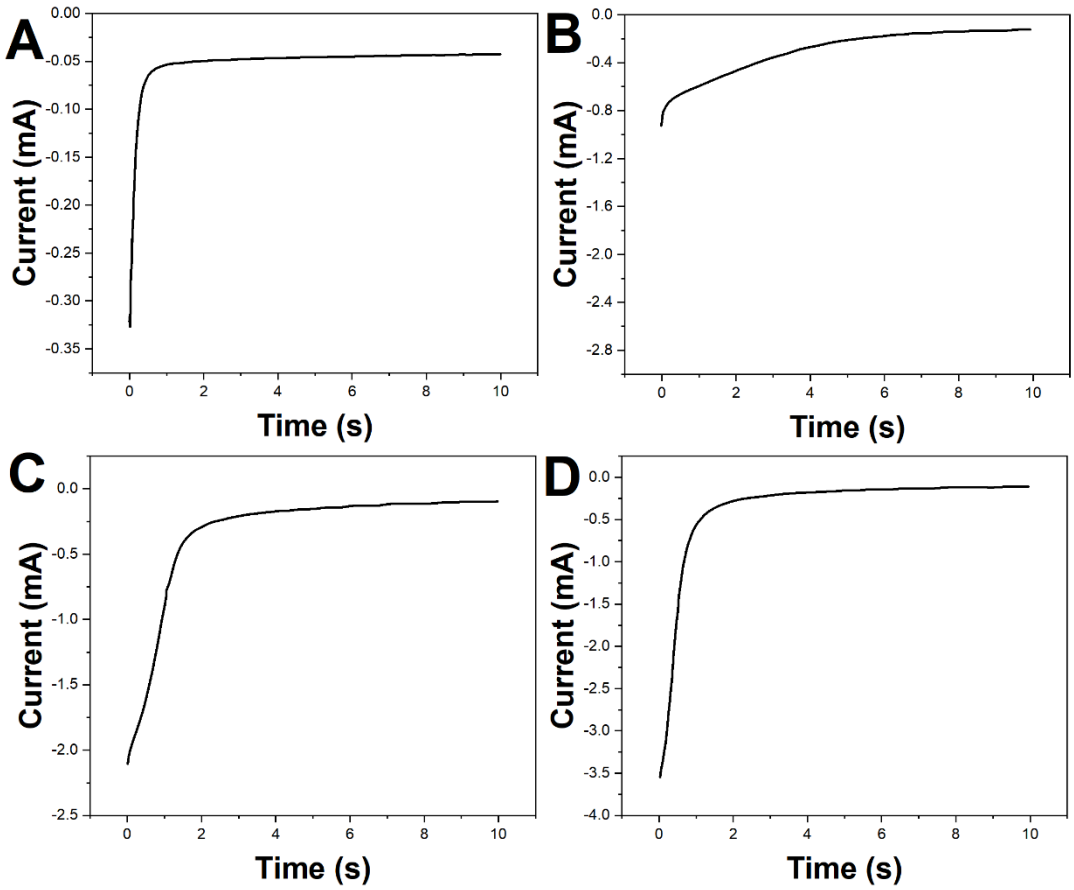

Figure 8. The step potential of -0.1 V, -0.2 V, -0.3 V and -0.4 V of PC in 0.1 M KOH.

4. CONCLUSION

In this study, a certain number of carbon microsphere structures were formed with phoenix tree leaves being the carbon source, and biomass carbon materials were prepared with hydrothermal methods. The carbon microspheres have a particle size of 2-4 μm and a certain degree of graphitization. KOH activated hydrothermal carbon materials and carbon materials with a honeycomb microporous structure on the surface were obtained. PC has a more graphitized degree and was applied to supercapacitor electrode materials, which exhibited good electrochemical performance. Electrochemical analysis show that the lower electrolyte carrier concentration seriously affects the capacitive performance of the material, and increasing the carrier concentration of the electrolyte can effectively improve the performance of the supercapacitor. PC has an oxygen reduction electrocatalytic activity similar to commercial 30 wt.%. It can be concluded that using PC as a fuel cell cathode material can simplify the structure of the energy subsystem of electric vehicles.

References

1. Y. Wang, L. Wang, M. Li, Z. Chen, *ETransportation*, 4 (2020) 100064.
2. V.K. Kasimalla, N.S. G., V. Velisala, *Int. J. Energy Res.*, 42 (2018) 4263–4283.
3. A. Kachhwaha, G.I. Rashed, A.R. Garg, O.P. Mahela, B. Khan, M.B. Shafik, M.G. Hussien, *Sustainability*, 14 (2022) 776.
4. H. Rezaei, S.E. Abdollahi, S. Abdollahi, S. Filizadeh, *J. Energy Storage*, 53 (2022) 105045.
5. I.-S. Sorlei, N. Bizon, P. Thounthong, M. Varlam, E. Carcadea, M. Culcer, M. Iliescu, M. Raceanu, *Energies*, 14 (2021) 252.
6. A. Prasanthi, H. Shareef, R. Errouissi, M. Asna, A. Mohamed, *Energy Convers. Manag. X*, 15 (2022) 100266.
7. P. Naresh, *J. Energy Storage*, 33 (2021) 102112.
8. M.S. Yadav, *J. Nanoparticle Res.*, 22 (2020) 367.
9. Z. Fu, L. Zhu, F. Tao, P. Si, L. Sun, *Int. J. Hydrog. Energy*, 45 (2020) 8875–8886.
10. H. Karimi-Maleh, M. Alizadeh, Y. Orooji, F. Karimi, M. Baghayeri, J. Rouhi, S. Tajik, H. Beitollahi, S. Agarwal, V.K. Gupta, S. Rajendran, S. Rostamnia, L. Fu, F. Saberi-Movahed, S. Malekmohammadi, *Ind. Eng. Chem. Res.*, 60 (2021) 816–823.
11. C. Wang, R. Xiong, J. Tian, J. Lu, C. Zhang, *Appl. Energy*, 305 (2022) 117819.
12. R. Xiong, H. Chen, C. Wang, F. Sun, *J. Clean. Prod.*, 202 (2018) 1228–1240.
13. H. Karimi-Maleh, A. Ayati, R. Davoodi, B. Tanhaei, F. Karimi, S. Malekmohammadi, Y. Orooji, L. Fu, M. Sillanpää, *J. Clean. Prod.*, 291 (2021) 125880.
14. Z. Du, C. Liu, J. Zhai, X. Guo, Y. Xiong, W. Su, G. He, *Catalysts*, 11 (2021) 393.
15. Y. Hames, K. Kaya, E. Baltacioglu, A. Turksoy, *Int. J. Hydrog. Energy*, 43 (2018) 10810–10821.
16. J. Shin, W.-S. Hwang, H. Choi, *Technol. Forecast. Soc. Change*, 143 (2019) 239–248.
17. Y. Manoharan, S.E. Hosseini, B. Butler, H. Alzhahrani, B.T.F. Senior, T. Ashuri, J. Krohn, *Appl. Sci.*, 9 (2019) 2296.
18. L. Ren, S. Zhou, X. Ou, *Energy*, 209 (2020) 118482.
19. A. Ajanovic, R. Haas, *Int. J. Hydrog. Energy*, 46 (2021) 10049–10058.
20. M.S. Bhaskar, V.K. Ramachandaramurthy, S. Padmanaban, F. Blaabjerg, D.M. Ionel, M. Mitolo, D. Almakhles, *IEEE Access*, 8 (2020) 178130–178166.
21. P. Ahmadi, S.H. Torabi, H. Afsaneh, Y. Sadegheih, H. Ganjehsarabi, M. Ashjaee, *Int. J. Hydrog. Energy*, 45 (2020) 3595–3608.
22. W. Zhang, J. Wang, D. Ruan, Q. Shi, F. Zhang, Q. Ren, Z. Shi, *Chem. Eng. J.*, 373 (2019) 1012–

1019.
23. K. Li, Q. Liu, H. Cheng, M. Hu, S. Zhang, *Spectrochim. Acta. A. Mol. Biomol. Spectrosc.*, 249 (2021) 119286.
24. H. Karimi-Maleh, C. Karaman, O. Karaman, F. Karimi, Y. Vasseghian, L. Fu, M. Baghayeri, J. Rouhi, P. Senthil Kumar, P.-L. Show, S. Rajendran, A.L. Sanati, A. Mirabi, *J. Nanostructure Chem.*, 12 (2022) 429–439.
25. X. Hu, L. Jia, J. Cheng, Z. Sun, *J. Hazard. Mater.*, 362 (2019) 1–8.
26. P. Boral, A.K. Varma, S. Maity, *Int. J. Coal Sci. Technol.*, 8 (2021) 1034–1053.
27. T. Petit, L. Puskar, *Diam. Relat. Mater.*, 89 (2018) 52–66.
28. H. Karimi-Maleh, F. Karimi, L. Fu, A.L. Sanati, M. Alizadeh, C. Karaman, Y. Orooji, *J. Hazard. Mater.*, 423 (2022) 127058.
29. L. Tao, X. Ma, L. Ye, J. Jia, L. Wang, P. Ma, J. Liu, *J. Anal. Appl. Pyrolysis*, 158 (2021) 105267.
30. H. Pu, S. Ruan, M. Yin, Q. Sun, Y. Zhang, P. Gao, X. Liang, W. Yin, H. Fa, *Microchem. J.*, 181 (2022) 107711.
31. A.L. Cazetta, T. Zhang, T.L. Silva, V.C. Almeida, T. Asefa, *Appl. Catal. B Environ.*, 225 (2018) 30–39.
32. Y. Guo, S. Yao, L. Gao, A. Chen, M. Jiao, H. Cui, Z. Zhou, *J. Mater. Chem. A*, 8 (2020) 4386–4395.
33. A. Chalgin, C. Song, P. Tao, W. Shang, T. Deng, J. Wu, *Prog. Nat. Sci. Mater. Int.*, 30 (2020) 289–297.
34. Y. Wu, Y. Chen, H. Wang, C. Wang, A. Wang, S. Zhao, X. Li, D. Sun, J. Jiang, *J. Mater. Chem. A*, 6 (2018) 12018–12028.
35. E.Y. Choi, D.E. Kim, S.Y. Lee, C.K. Kim, *Carbon*, 166 (2020) 245–255.
36. W. Niu, K. Marcus, L. Zhou, Z. Li, L. Shi, K. Liang, Y. Yang, *ACS Catal.*, 8 (2018) 1926–1931.
37. M. Abdinejad, C. Dao, X.-A. Zhang, H.B. Kraatz, *J. Energy Chem.*, 58 (2021) 162–169.
38. W. Yan, Y. Wu, Y. Chen, Q. Liu, K. Wang, N. Cao, F. Dai, X. Li, J. Jiang, *J. Energy Chem.*, 44 (2020) 121–130.
39. Y.-J. Song, J.-T. Ren, G. Yuan, Y. Yao, X. Liu, Z.-Y. Yuan, *J. Energy Chem.*, 38 (2019) 68–77.
40. M. Qiao, S.S. Meysami, G.A. Ferrero, F. Xie, H. Meng, N. Grobert, M. Titirici, *Adv. Funct. Mater.*, 28 (2018) 1707284.
41. M. Tavakkoli, E. Flahaut, P. Peljo, J. Sainio, F. Davodi, E.V. Lobiak, K. Mustonen, E.I. Kauppinen, *ACS Catal.*, 10 (2020) 4647–4658.
42. W. Si, Z. Yang, X. Hu, Q. Lv, X. Li, F. Zhao, J. He, C. Huang, *J. Mater. Chem. A*, 9 (2021) 14507–14514.
43. J. Masa, W. Schuhmann, *ChemCatChem*, 11 (2019) 5842–5854.
44. P. Wang, Q. Wang, G. Zhang, H. Jiao, X. Deng, L. Liu, *J. Solid State Electrochem.*, 20 (2016) 319–325.
45. B. Wang, Y. Wang, Y. Peng, X. Wang, J. Wang, J. Zhao, *J. Power Sources*, 390 (2018) 186–196.
46. Q. Zhang, K. Han, S. Li, M. Li, J. Li, K. Ren, *Nanoscale*, 10 (2018) 2427–2437.
47. Y. Zhang, M. Jia, J. Yu, J. Fan, L. Wang, Y. Zou, Y. Zhao, *J. Solid State Electrochem.*, 20 (2016) 733–741.
48. X. Lv, J. Ren, Y. Wang, Y. Liu, Z.-Y. Yuan, *ACS Sustain. Chem. Eng.*, 7 (2019) 8993–9001.
49. N.A. Galiote, F. Oliveira, F.H.B. de Lima, *Appl. Catal. B Environ.*, 253 (2019) 300–308.
50. W. Li, L. Huang, T. Wang, X. Hao, B. Wang, Q. Lu, X. Liang, F. Liu, F. Liu, C. Wang, *Sens. Actuators B Chem.*, 346 (2021) 130543.
51. S. Shen, F. Li, L. Luo, Y. Guo, X. Yan, C. Ke, J. Zhang, *J. Electrochem. Soc.*, 165 (2018) D43.
52. S. Chung, K. Ham, S. Kang, H. Ju, J. Lee, *Electrochimica Acta*, 348 (2020) 136346.
53. R. Tian, S. Shen, F. Zhu, L. Luo, X. Yan, G. Wei, J. Zhang, *ChemSusChem*, 11 (2018) 1015–1019.
54. Z. Ma, Z. Li, S. Li, P. Li, H. Zhang, *Mater. Lett.*, 229 (2018) 148–151.
55. Y. Nakazato, D. Kawachino, Z. Noda, J. Matsuda, S.M. Lyth, A. Hayashi, K. Sasaki, *J. Electrochem. Soc.*, 165 (2018) F1154.

56. S. Matsumoto, M. Nagamine, Z. Noda, J. Matsuda, S.M. Lyth, A. Hayashi, K. Sasaki, *J. Electrochem. Soc.*, 165 (2018) F1164.
57. K. Agrawal, A.A. Naik, S. Chaudhary, D. Parvatalu, V. Santhanam, *Chem. Asian J.*, 16 (2021) 3311–3325.
58. E.O. Nwanebu, N. Abou Harb, R. Gharbi, S. Omanovic, *Solid State Sci.*, 119 (2021) 106703.